

DAFNe: A One-Stage Anchor-Free Approach for Oriented Object Detection

Steven Lang,¹ Fabrizio Ventola,¹ Kristian Kersting^{1,2}

¹ TU Darmstadt, Darmstadt, Germany

² Hessian Center for AI and Centre for Cognitive Science, Darmstadt, Germany
{steven.lang, ventola, kersting}@cs.tu-darmstadt.de



Figure 1: Comparison of axis-aligned (top) and oriented (bottom) bounding box detections obtained with our model on aerial view imagery from DOTA 1.0. Clearly, the oriented bounding box representation is a generalization of horizontal bounding boxes and therefore a better choice for oriented objects. It generates tighter boxes that better cover and fit the true area of the object.

Abstract

We present DAFNe, a Dense one-stage Anchor-Free deep Network for oriented object detection. As a one-stage model, it performs bounding box predictions on a dense grid over the input image, being architecturally simpler in design, as well as easier to optimize than its two-stage counterparts. Furthermore, as an anchor-free model, it reduces the prediction complexity by refraining from employing bounding box anchors. With DAFNe we introduce an orientation-aware generalization of the center-ness function for arbitrarily oriented bounding boxes to down-weight low-quality predictions and a center-to-corner bounding box prediction strategy that improves object localization performance. Our experiments show that DAFNe outperforms all previous one-stage anchor-free models on DOTA 1.0, DOTA 1.5, and UCAS-AOD and is on par with the best models on HRSC2016.

1 Introduction

Object detection is one of the fundamental tasks in computer vision that is needed to develop intelligent systems which aim to understand the visual world. The task of object detection is to answer two main questions: *Where* are visual objects of interest located in a given image (object localization)? *What* are these objects (object recognition)?

Both questions are tightly coupled as we first need to understand where to look before asking what we are looking at. Many computer vision problems depend on object detection as a basis: Object tracking (Kang et al. 2018) performs object detection in a sequence of images and matches the corresponding objects across time, instance segmentation (Dai, He, and Sun 2016; Hariharan et al. 2014, 2015; He et al. 2017) predicts labels of different object instances pixel-wise, image captioning (Karpathy and Fei-Fei 2015; Wu et al. 2018; Xu et al. 2015) generates a textual description of the image content. Recently, a generalization of object detection has emerged: oriented object detection. Here, the localization extends to arbitrarily oriented objects by taking the object orientation into account. As demonstrated in Figure 1, oriented bounding boxes are a generalization of horizontal bounding boxes and can tightly fit objects with dense object distributions and arbitrary orientations.

As with several tasks in machine learning, the rise of deep learning (Goodfellow, Bengio, and Courville 2016) in recent years has pushed the boundaries in computer vision far beyond what was prior state-of-the-art. Most successful deep architectures for object detection such as Faster R-CNN (Ren et al. 2015), SSD (Liu et al. 2016), and YOLOv2,v3 (Redmon and Farhadi 2017, 2018) are based on a technique that includes prior information about possible object sizes and aspect ratios. These are called bounding box priors or *anchor boxes* which need to be handcrafted and can vary for different datasets, introducing many additional hyper-parameters to be tuned for a single dataset. On the other side, humans can localize objects without pre-defined templates. Motivated by this idea, anchor-free approaches forgo prior information about possible bounding boxes and, thus, they get rid of the additional hyper-parameters and reduce the computational complexity. This is the direction taken by UnitBox (Yu et al. 2016), YOLOv1 (Redmon et al. 2016), CenterNet (Duan et al. 2019), CornerNet (Law and Deng 2019), ExtremeNet (Zhou, Zhuo, and Krähenbühl 2019), FoveaBox (Kong et al. 2019), and FCOS (Tian et al. 2019), to name a few. Moreover, object detection approaches can be divided into two main categories. The first includes those methods that are based on a *two-stage* architecture, where the first stage generates regions of interest proposals where possible objects could be located, while the second stage takes each proposal separately, fine-tunes the localiza-

tion, and classifies the object. The second category consists of *one-stage* methods such as RetinaNet (Lin et al. 2020), SSD (Liu et al. 2016), YOLOv1,v2,v3 (Redmon et al. 2016; Redmon and Farhadi 2017, 2018), which get rid of the region proposal stage and perform the localization and classification directly on a dense grid of possible locations in a single pass. As shown in RetinaNet (Lin et al. 2020), these can achieve competitive accuracy while being faster than their two-stage alternatives.

Oriented object detection has been approached mainly by two-stage anchor-based models in the past, while only a few works have focused on the faster and conceptually simpler one-stage anchor-free models. In this work, our goal is to approach oriented object detection with a one-stage anchor-free deep model, taking advantage of their simpler design and reduced computational requirements. To this aim, inspired by the success of prominent one-stage anchor-free models from horizontal object detection, we introduce DAFNe, a novel dense one-stage anchor-free approach for oriented object detection. Moreover, we propose an orientation-aware generalization of the center-ness function presented in FCOS (Tian et al. 2019) to focus on predictions that are closer to an oriented object’s center. We also enhance the detector’s localization performance by introducing a novel center-to-corner bounding box regression to reframe the corner regression by separating it into an easier object-center prediction and a subsequent center-to-corner prediction step. These contributions can improve the model’s detection accuracy outperforming, to the best of our knowledge, all one-stage anchor-free models in the literature on the most common benchmarks. To summarize, our contributions are the following:

- We introduce DAFNe, a novel one-stage anchor-free deep model for oriented object detection that, to date, is the most accurate one-stage anchor-free architecture for this task.
- We present the first generalization of the center-ness function to arbitrary quadrilaterals that take into account the object’s orientation and that accurately down-weights low-quality predictions.
- We reframe the corner regression following a divide-and-conquer strategy, i.e. we divide it into an easier object-center prediction step followed by a center-to-corner prediction to improve object localization performance.

2 Related Work

Due to their success in horizontal object detection, the vast majority of the work on oriented object detection has focused on two-stage anchor-based architectures (Ding et al. 2019; Chen et al. 2017; Li et al. 2019a; Liu, Pan, and Lei 2017; Ma et al. 2018; Yang et al. 2020). Later contributions have shifted from two-stage to one-stage models, taking advantage of their architectural and procedural simplicity. Here we briefly introduce the most relevant anchor-based and anchor-free one-stage models in the literature.

One-Stage Oriented Object Detection: Anchor-Based Methods

The first relevant work on one-stage anchor-based oriented object detection introduces the Saliency Biased Loss (Sun et al. 2018), which is a loss function based on saliency information directly extracted from the input image. This is similar in spirit to the Focal Loss in RetinaNet (Lin et al. 2020), as it treats training samples differently according to their complexity (saliency). This is estimated by an additional deep model trained on ImageNet (Deng et al. 2009) where the number of active neurons across different convolution layers is measured. The concept is that with increasing complexity, more neurons would be active. The saliency then scales an arbitrary base loss function to adapt the importance of training samples accordingly.

The work by Han et al. (Han et al. 2021a) (S2ANet) attempts to improve the discrepancy of classification score and localization accuracy and ascribes this issue to the misalignment between anchor boxes and the axis-aligned convolutional features. Hence, the authors propose two modules. The first one generates high quality-oriented anchors using their Anchor Refinement Network which adaptively aligns the convolutional features according to the generated anchors using an Alignment Convolution Layer. The second module adopts Active Rotating Filters (Zhou et al. 2017) to encode the orientation context and it produces orientation-aware features to alleviate classification score and localization accuracy inconsistencies.

In R³Det (Yang et al. 2021a), the authors propose a progressive regression approach from coarse to fine granularity, introducing a feature refinement module that re-encodes the current refined bounding box to the corresponding feature points through pixel-wise feature interpolation, realizing feature reconstruction and alignment.

Besides, the solution devised by Yang et al. (Yang and Yan 2020) tackles the issue of discontinuous boundary effects on the loss due to the inherent angular periodicity and corner ordering by transforming the angular prediction task from a regression problem into a classification problem. The authors conceived the Circular Smooth Label technique which handles the periodicity of angles and raises the error lenience to adjacent angles.

One-Stage Oriented Object Detection: Anchor-Free Methods

The first one-stage anchor-free oriented object detector, IENet (Lin, Feng, and Guan 2019), is based on the one-stage anchor-free fully convolutional detector FCOS. The regression head from FCOS is extended by another branch that regresses the bounding box orientation, using a self-attention mechanism that incorporates the branch feature maps of the object classification and box regression branches.

In Axis-Learning (Xiao et al. 2020), the authors also build on the dense sampling approach of FCOS and explore the prediction of an object axis, defined by its head point and tail point of the object along its elongated side (which can lead to ambiguity for near-square objects). The axis is extended by a width prediction which is interpreted to be orthogonal

to the object axis. Similar to our work, Xiao et al. (Xiao et al. 2020) further introduce an orientation adjusted formulation for rectangular bounding boxes of the center-ness function, proposed by FCOS, which is scaled by the bounding box aspect ratio to take objects with heavily skewed aspect ratios into account.

In PIoU (Chen et al. 2020) the authors argue that a distance-based regression loss such as SmoothL1 only loosely correlates to the actual Intersection over Union (IoU) measurement, especially in the case of large aspect ratios. Therefore, they propose the Pixels-IoU (PIoU) loss, which exploits the IoU for optimization by pixel-wise sampling, dramatically improving detection performance on objects with large aspect ratios.

P-RSDet (Zhou et al. 2020b) replaces the Cartesian coordinate representation of bounding boxes with polar coordinates. Therefore, the bounding box regression happens by predicting the object’s center point, a polar radius, and two polar angles. Furthermore, they introduce the Polar Ring Area Loss to express the geometric constraint between the polar radius and the polar angles.

Another alternative formulation of the bounding box representation is defined in O^2 -DNet (Wei et al. 2020). Here, oriented objects are detected by predicting a pair of middle lines inside each target, similar to the extreme keypoint detection schema proposed in ExtremeNet (Zhou, Zhuo, and Krähenbühl 2019).

3 DAFNe: A One-Stage Anchor-Free Approach for Oriented Object Detection

Oriented object detection has been mainly tackled by the adaption of two-stage anchor-based models, which come with increased methodological and computational complexity. In this work, we take a different path and propose DAFNe, an oriented object detector, devising a one-stage anchor-free architecture that is simpler and faster in concept compared to its two-stage anchor-based alternatives. We employ RetinaNet (Lin et al. 2020) as the base architecture, which is composed of a ResNet (He et al. 2016) backbone combined with a Feature Pyramid Network (FPN) (Lin et al. 2017) as multi-scale feature extractor on top which produces feature maps at five scales (see Appendix A for the architecture schematic). The different feature maps are then fed into a prediction head, consisting of two sequential convolution branches for classification and regression respectively. To regress oriented bounding boxes, we construct relative targets such that

$$\mathbf{t}^* \leftarrow (x_0^* - x, y_0^* - y, x_1^* - x, y_1^* - y, x_2^* - x, y_2^* - y, x_3^* - x, y_3^* - y) / s, \quad (1)$$

where (x_i^*, y_i^*) are the absolute corner coordinates of the original target bounding box, (x, y) is a location in the regression branch feature map and $s = 2^l$ is the output stride of level l of the FPN feature map. Thus, the target bounding boxes are then represented as scale-normalized offsets from locations w.r.t. the output feature map. For further architectural, training, and inference details we refer the reader to RetinaNet (Lin et al. 2020) and FCOS (Tian et al. 2019).

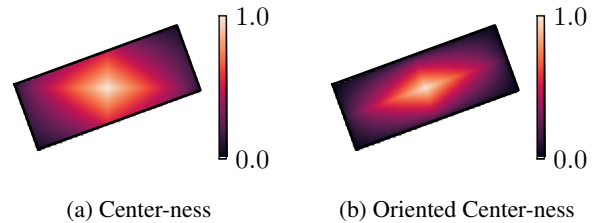


Figure 2: Function evaluation of every location in a given oriented bounding box w.r.t. the original center-ness (a) and the proposed oriented center-ness (b). It is clear that the original center-ness function does not adapt well to oriented bounding boxes. On the contrary, the proposed oriented center-ness aligns to arbitrary edge orientations and it can take heavily skewed aspect ratios into account as well.

Oriented Center-Ness

FCOS (Tian et al. 2019) has introduced the *center-ness* prediction which depicts the normalized distance from the feature map location to the center of the target object, for which the location is responsible. Since center-ness has been formulated in the task of classic horizontal object detection and it is measured w.r.t. axis-aligned edges, it does not directly translate to oriented bounding boxes when applied to their axis-aligned hull (see Figure 2a).

Therefore, we propose a generalization of the center-ness formulation to arbitrary quadrilaterals by measuring the normalized perpendicular distances between any feature map location (x, y) and the edge between two subsequent corners (p_x^0, p_y^0) and (p_x^1, p_y^1) in the oriented bounding box:

$$\text{dist}(p_x^0, p_y^0, p_x^1, p_y^1, x, y) = \frac{|(p_x^1 - p_x^0)(p_y^0 - y) - (p_x^0 - x)(p_y^1 - p_y^0)|}{\sqrt{(p_x^1 - p_x^0)^2 + (p_y^1 - p_y^0)^2}}. \quad (2)$$

With this, we can obtain the four perpendicular distances a, b, c, d of a given oriented bounding box $(x_0, y_0, x_1, y_1, x_2, y_2, x_3, y_3)$:

$$\begin{aligned} a &= \text{dist}(x_0, y_0, x_1, y_1, x, y), \\ b &= \text{dist}(x_1, y_1, x_2, y_2, x, y), \\ c &= \text{dist}(x_2, y_2, x_3, y_3, x, y), \\ d &= \text{dist}(x_3, y_3, x_0, y_0, x, y). \end{aligned} \quad (3)$$

The oriented center-ness is then calculated with

$$\text{center-ness}(a, b, c, d) = \left(\frac{\min(a, c)}{\max(a, c)} \cdot \frac{\min(b, d)}{\max(b, d)} \right)^{\frac{1}{\alpha}}, \quad (4)$$

where the hyper-parameter α controls the decay rate of the center-ness. Figure 2b shows the oriented center-ness heatmap for each location in the given oriented bounding box. One can see that the function now aligns perfectly with the box edges and adapts to its aspect ratio whereas the original center-ness formulation depicted in Figure 2a fails to do so. The center-ness value ranges from 0 to 1, corresponding

to the location being on the edge or in the center of the box respectively.

The goal of oriented center-ness is to down-weight classification scores of predicted low-quality bounding boxes and, thus, removing them during post-processing steps such as confidence thresholding and non-maximum suppression. In this context, a low-quality bounding box is defined as a prediction with high confidence but low overlap with the ground-truth bounding box which possibly leads to false positives and, consequently, reduces the detectors precision (Tian et al. 2019).

The oriented center-ness is predicted using an additional 3×3 convolution with a single output channel on top of the regression branch. During testing, the final score $s_{x,y}$, used for ranking detections during non-maximum suppression is obtained by adjusting the classification confidence $p_{x,y}$ with the predicted oriented center-ness $o_{x,y}$ at location (x, y) : $s_{x,y} = \sqrt{p_{x,y} \cdot o_{x,y}}$.

Another modification of the center-ness function to oriented bounding boxes has been proposed in Axis-Learning (Xiao et al. 2020). It is limited to oriented rectangles and not normalized, i.e. depending on the object aspect ratio, it can exceed values of 1. In contrast, our formulation generalizes to arbitrary quadrilaterals and it is constrained to be in $[0, 1]$.

Corner Prediction Strategies

Traditionally, in horizontal and oriented object detection, the bounding box regression is performed in a single step, i.e. the last feature map of the regression branch predicts all coordinates at a specific feature location at once. This is shown in Figure 3a where each corner is predicted as an offset from the location (orange dot). In this work, we explore the idea of separating the prediction of corners into multiple steps, by introducing direct dependencies between the intermediate steps. To the best of our knowledge, no previous work has explored and analyzed the impact of dividing the bounding box prediction into multiple interdependent parts. We compare the baseline of “direct” box predictions to a naive single-anchor-based approach named “offset” depicted in Figure 3b, as well as to two prediction strategies we introduce, i.e. “iterative” and “center-to-corner”.

The “iterative” prediction strategy is inspired by the decomposition of a joint probability distribution into conditionals using the chain rule. This leads to an iterative prediction strategy where each corner is predicted using the previous corners as shown in Figure 3c:

$$\begin{aligned} c_0 &= \text{conv}_{256 \rightarrow 2}(\mathbf{X}) \\ c_1 &= \text{conv}_{258 \rightarrow 2}(\mathbf{X}, c_0) \\ c_2 &= \text{conv}_{260 \rightarrow 2}(\mathbf{X}, c_0, c_1) \\ c_3 &= \text{conv}_{262 \rightarrow 2}(\mathbf{X}, c_0, c_1, c_2), \end{aligned} \quad (5)$$

where $\text{conv}_{ic \rightarrow oc}$ represents a 3×3 convolution with ic input channels and oc output channels. The idea is that with more information available, following corners can be predicted more consistently w.r.t. the previous ones. As an extreme example, knowing the first three corners and predicting the fourth from those should be easier than predicting

the fourth corner without prior knowledge about where the other corners are (under the assumption that this is not already encoded in the incoming features which are used to predict the others).

The second proposal, the “center-to-corner” strategy, is to split the prediction into two phases. The first phase predicts the center of the object while the second phase regresses the corners from the predicted center (see Figure 3d). For this, the regression branch is divided into two separate branches, namely the center branch responsible for the object’s center prediction and the corner branch responsible for the center-to-corner offset prediction.

$$\tilde{c} = \text{center-branch}_{256 \rightarrow 2}(\mathbf{X})$$

$$c_0, c_1, c_2, c_3 = \text{corner-branch}_{256 \rightarrow (4 \times 2)}(\mathbf{X}) + \tilde{c}. \quad (6)$$

Note that $+$ in (6) is a broadcasting operation and adds the center prediction \tilde{c} to each tuple of the corner branch output. In addition, the center prediction is also used during the optimization, such that the center is not only indirectly optimized using the corners as a proxy but also directly, by employing a loss w.r.t. the target object center. This strategy is inspired by the general concept of divide-and-conquer. In fact, the task of predicting the center is easier than the task of predicting all four corners as it is lower-dimensional and is independent of the object’s width, height, and orientation. Therefore, the model can first focus on getting the general location of an object right by optimizing the center loss and, then, gradually refine the corners from the predicted center.

Learning Objectives

We follow RetinaNet (Lin et al. 2020) for the choice of learning objectives. That is, the Focal Loss is employed for classification to down-weight the contribution of objects that are easy to classify and shift the training focus on objects that are predicted with low confidences. For the regression of oriented bounding box coordinates, we adopt the SmoothL1 loss over the difference between the predicted and the target coordinates. To increase training stability, we use the eight-point loss modulation proposed by Qian et al. (Qian et al. 2021). As in FCOS, the oriented center-ness is interpreted as the likelihood of the responsibility of the current location w.r.t. the target. Thus, the binary cross-entropy loss is used as the oriented center-ness optimization objective.

4 Experimental Evaluation

In this section, we empirically evaluate our contributions and show how they can be beneficial for oriented object detection. We run experiments to answer the following questions: (Q1) Does the proposed oriented center-ness improve accuracy? (Q2) Do the introduced corner prediction strategies perform better than the approach commonly used in the literature? (Q3) Does DAFNe, together with oriented center-ness and center-to-corner prediction strategy, improve the state-of-the-art accuracy for one-stage anchor-free oriented object detection?

Experimental Setup

Dataset. The experiments are conducted on HRSC2016 (Liu et al. 2017), UCAS-AOD (Li et al.

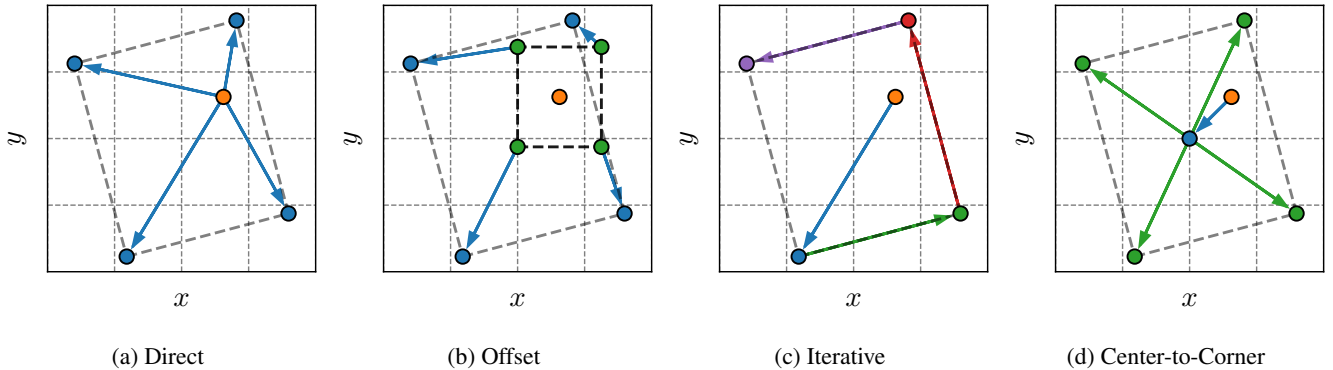


Figure 3: The baseline (a) and the proposed (b), (c), and (d) corner prediction strategies. In (a), the four corners are obtained by predicting four vectors as an offset from the current location. (b) resembles an anchor-based approach with a single base anchor, it predicts the corners as offsets for each corner of the anchor. In (c), each corners is obtained by taking the previous corner into consideration. In (d), first the center is predicted as an offset from the location, then, the corners are predicted as an offset from the predicted center.

2019b)¹, DOTA 1.0 (Xia et al. 2018), and DOTA 1.5 datasets. For DOTA 1.0 and 1.5 we pre-process each image into patches of 1024×1024 pixels with an overlap of 200 pixels between patches. Online data augmentation is applied during training. Specifically, we perform random horizontal and vertical flipping with a chance of 50%. Additionally, the images are rotated by either 0° , 90° , 180° or 270° with equal chance. As commonly done in practice, for our final results (Table 3) we train the model on the joint of train and validation set, increase the number of training iterations by a factor of 3, train on image patches of multiple patch-sizes (600, 800, 1024, 1300, 1600) on DOTA, and adopt multi-scale train and test-time augmentation (450, 500, 600, 700, 800, 900, 1000, 1100, 1200). As an accuracy measurement, we adopt the mean Average Precision (mAP) evaluation metric.

Training and Inference. We employ ResNet-50 as the backbone model unless otherwise specified. The backbone weights are initialized from a pre-trained ResNet-50 on ImageNet. All other model weights are initialized as in RetinaNet (Lin et al. 2020). The model is optimized using SGD for 90k iterations with a base learning rate of 0.01 and a batch size of 8 images. The learning rate is reduced by a factor of 10 after 60k and 80k iterations. Inspired by Goyal et al. (Goyal et al. 2018), we employ a warm-up phase of 500 iterations with linear scaling of the learning rate starting from 0.001 to 0.01 to overcome optimization difficulties in early training. The weight-decay and momentum optimization techniques are applied with values of 0.0001 and 0.9 respectively. The loss function hyper-parameters were adapted from RetinaNet without further tuning, i.e. for Focal Loss we set $\alpha = 0.25$ and $\gamma = 2.0$, while for SmoothL1 loss we set $\beta = 1/9$. To account for the magnitude discrepancy between the classification and regression loss, the classifi-

cation loss weight is set to $\lambda_{cls} = 10$ and for all other loss terms we set $\lambda_i = 1$. Additionally, all loss weights were normalized setting $\lambda_i = \lambda_i / \sum_j \lambda_j$. At test time, predictions with a confidence $p < 0.05$ are removed. Furthermore, we apply a *top-k* class-confidence filtering with $k = 2000$. For non-maximum suppression, we set the threshold t_{nms} for overlapping boxes of the same class to 0.1. All experiments were run on NVIDIA DGX-2 systems, using four V100 (32GB VRAM) GPUs.

(Q1) Oriented Center-Ness Improves Accuracy

We compare DAFNe with the proposed oriented center-ness against DAFNe without center-ness and against DAFNe with axis-aligned center-ness (by using the axis-aligned hull of the oriented bounding box). For this comparison, we employ the direct corner prediction strategies on all models. Table 1 shows that the oriented center-ness consistently improves the model’s performance on all datasets. We observed that different values for α are optimal for different datasets ($\alpha = 4, 3, 5, 2$ for DOTA 1.0, DOTA 1.5, UCAS-AOD, and HRSC2016 respectively). A larger value of α leads to a slower decay of the oriented center-ness value, starting from 1 in the center of the object to 0 at the object’s boundaries. Since the predicted center-ness is used to adjust the classification confidence value, α effectively controls the penalty that off-center predictions receive. Thus, the proposed oriented center-ness improves the validation mAP score by assigning low scores to off-center predictions that are removed afterward, during post-processing steps.

To better understand the improvement that the oriented center-ness adjustment to the classification confidence achieves, we have collected the true positive detections on DOTA 1.0 as a heatmap in Figure 4 (see Appendix B for a class-based separation of this heatmap). Here, the classification confidences of the detections are drawn against the IoU with the ground-truth bounding box. That is, given a trained model, for each correctly detected oriented bounding box in the validation set, a pair of (*confidence*, *IoU*)

¹For the UCAS-AOD benchmark we use the predefined split from <https://github.com/ming71/UCAS-AOD-benchmark> to ensure comparability between results.

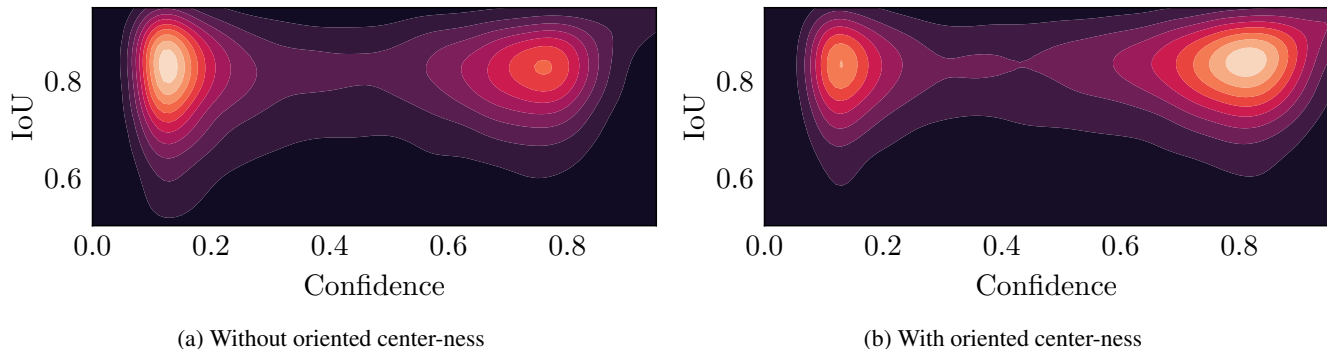


Figure 4: Density of classification confidences against IoU values for correctly detected (true positives) oriented bounding boxes on DOTA 1.0 validation set. Predictions adjusted with oriented center-ness lead to higher classification confidence. As a result, accuracy is improved since detections with low center-ness values are successfully removed during post-processing steps such as confidence thresholding and non-maximum suppression.

Table 1: Influence of the center-ness function on accuracy (mAP) on the validation set of HRSC2016, UCAS-AOD, DOTA 1.0, and DOTA 1.5. The introduced oriented center-ness function consistently improves model accuracy on all datasets

| | Center-ness | HRSC2016 | UCAS-AOD | DOTA 1.0 | DOTA 1.5 |
|----------|--------------|--------------|--------------|--------------|--------------|
| Baseline | none | 61.68 | 89.83 | 69.97 | 68.91 |
| | axis-aligned | 70.30 | 89.97 | 69.95 | 67.98 |
| Ours | oriented | 78.87 | 90.03 | 71.17 | 70.09 |

is collected, where the IoU is computed between the predicted bounding box and the ground-truth bounding box. The heatmap brightness indicates the density of correctly detected objects in the validation dataset. The classification confidences in the heatmap of Figure 4a are obtained without employing oriented center-ness, while confidences in the heatmap of Figure 4b are obtained by employing oriented center-ness (note that the values used for the heatmaps are the confidences p and not the center-ness adjusted scores s). The inclusion of oriented center-ness as an adjustment to the classification confidence results in detections of higher confidences. Consequently, the detections with low center-ness values are successfully removed during post-processing steps such as score thresholding and non-maximum suppression. Thus, we can answer (Q1) affirmatively, the proposed oriented center-ness is beneficial for the model accuracy.

(Q2) Corner Prediction Strategies to Improve Detection

As aforementioned, the use of a quadrilateral representation for oriented bounding boxes provides additional freedom in the way the regression head can produce the final corners. We compare the performance of the different corner prediction strategies we have introduced against the “direct” strategy, i.e. the de facto standard approach in object detection. Table 2 reports the experimental results obtained on the validation sets for each prediction strategy with DAFNe (without employing the oriented center-ness). When compared to the direct strategy, the center-to-corner strategy improves

performance on all datasets, by 0.14%, 0.50%, 1.76%, and 4.09% mAP for UCAS-AOD, DOTA 1.5, DOTA 1.0, and HRSC2016 respectively. The offset and iterative prediction strategies lead to mixed results, turning the center-to-corner strategy into the best choice since it outperforms the other introduced strategies on UCAS-AOD, HRSC2016, and DOTA 1.0 and it is on par on DOTA 1.5. This suggests that the division of predicting the object’s center first and the offset to its corners afterward does lead to better object localization. However, the center-to-corner approach introduces a second branch, namely the center regression branch, and thus, it requires 2.4M additional parameters. Therefore, we investigate whether the increased model capacity is the reason for this improvement. We evaluate the model on DOTA 1.0 using the direct corner prediction strategy and modulate the tower’s capacity by increasing the number of convolution layers in the prediction branches from 1 to 8, resulting in an increase of 1.2M parameters per layer. As one can see in Figure 5, the best model achieved 70.10% mAP (3 convolution layers), while the others performed slightly worse. Thus, simply increasing the tower’s capacity does not lead to better model accuracy. The improvement observed with the center-to-corner regression approach shows that it is a valid methodological advancement over the direct corner regression. In summary, we can answer (Q2) positively, the introduced divide-and-conquer corner prediction strategies outperform the direct approach. The center-to-corner is, in general, the best choice.

Table 2: Comparison of the proposed divide-and-conquer corner prediction strategies with the direct strategy, i.e. the de facto standard approach. Results are obtained on the validation sets. Center-to-corner is overall the best strategy. It outperforms the baseline (direct) strategy on every dataset (noted with \uparrow) and it outperforms the other novel methods we introduced except on DOTA 1.5, where it is on par with them

| | Strategy | HRSC2016 | UCAS-AOD | DOTA 1.0 | DOTA 1.5 |
|----------|------------------|-----------------------------------|-----------------------------------|-----------------------------------|------------------|
| Baseline | direct | 61.68 | 89.83 | 69.97 | 68.91 |
| Ours | offset | 64.84 | 89.95 | 71.10 | 69.88 |
| | iterative | 55.24 | 89.89 | 71.72 | 69.68 |
| | center-to-corner | 65.77\uparrow | 89.97\uparrow | 71.73\uparrow | 69.41 \uparrow |

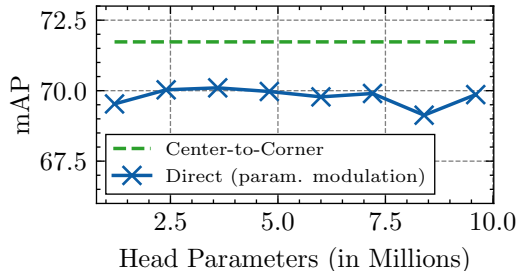


Figure 5: Modulation of the number of head convolutions for the classification and bounding box regression branches with the “direct” corner prediction strategy on the DOTA 1.0 validation set. Simply increasing the model capacity does not lead to the same improvements in accuracy as obtained with the introduced “center-to-corner” strategy.

(Q3) DAFNe: The State-of-the-Art for One-Stage Anchor-Free Oriented Object Detection

One-stage anchor-free, as well as oriented object detection, are relatively new in the field of computer vision. Only little research has been done at their intersection. We compare DAFNe equipped with oriented center-ness, center-to-corner prediction strategy, and the learning objectives as described before with all other one-stage anchor-free methods in the literature, to the best of our knowledge. Moreover, we compare it with the most prominent two-stage and anchor-based approaches in the literature employed as gold standard. Models are evaluated on the test sets of UCAS-AOD, HRSC2016, DOTA 1.0, DOTA 1.5. In Table 3a we show that DAFNe outperforms all previous one-stage anchor-free models on DOTA 1.0 by a large margin, setting the new state-of-the-art result of 76.95% mAP. For a comprehensive class-separated evaluation on DOTA 1.0, see Appendix C. On HRSC2016 (Table 3b), DAFNe performs close to the current best model, CenterRot (Wang, Yang, and Li 2021). Since no other one-stage anchor-free model has been evaluated on DOTA 1.5 (Table 3c), we set a new baseline of 71.99% mAP. We outperform R-RetinaNet on UCAS-AOD (Table 3d) by 2.28% mAP and perform only 0.14% mAP below the state-of-the-art result for *anchor-based* models (S2ANet, 89.99% mAP). In general, being more accurate, DAFNe reduces the gap with more complex two-stage and

anchor-based models. Therefore, we can answer (Q3) affirmatively, DAFNe sets the new state-of-the-art accuracy for one-stage anchor-free oriented object detection.

5 Conclusion

In this work, we have introduced DAFNe, a one-stage anchor-free approach for oriented object detection, a central task in computer vision. Taking into account the orientation of both the objects and the bounding boxes makes oriented object detection a more general and, thus, a harder task than the simpler horizontal one. Compared to two-stage anchor-based solutions, DAFNe is simpler in design, faster, and easier to optimize, and it does not need data-specific anchors. To overcome the additional challenges of oriented object detection, next to presenting DAFNe’s design and learning objectives that foster training stability, we have introduced a novel oriented center-ness and new divide-and-conquer corner prediction strategies. We have demonstrated how our oriented center-ness substantially improves accuracy. Moreover, we have shown that more advanced corner prediction strategies can improve localization performance, with the proposed “center-to-corner” strategy consistently outperforming the “direct” baseline strategy. Potentially, these can be beneficial also for the horizontal case. With these contributions, we have set the new state-of-the-art accuracy for one-stage anchor-free oriented object detection on the DOTA 1.0, DOTA 1.5, and UCAS-AOD benchmarks and perform on par with the previous best models on HRSC2016. Since recent anchor-based models are currently the gold standard in terms of accuracy, DAFNe presents a step forward to close the gap with these more complex solutions.

Acknowledgements

This work was supported by the Federal Ministry of Education and Research (BMBF) Competence Center for AI and Labour “kompAKI” (FKZ 02L19C150), the German Science Foundation (DFG, German Research Foundation; GRK 1994/1 “AIPHES”), and the Hessian Ministry of Higher Education, Research, Science and the Arts (HMWK) project “The Third Wave of AI”.

Table 3: Test set accuracies (in mAP) of DAFNe compared with all other one-stage anchor-free oriented object detection models in the literature and with more complex two-stage and anchor-based models. Note that “*” indicates multi-scale training and testing, and “†” indicates a two-stage model. We abbreviate backbone architectures with R(X)-50/101/152 as ResN(X)et-50/101/152, HG-104 as Hourglass-104, and DN-53 as Darknet-53. Prefix “Re” indicates a rotation-equivariant architecture. Best results in bold, our approach is highlighted

| (a) Evaluation on DOTA 1.0 | | | (b) Evaluation on HRSC2016 | | |
|--|--------------------------------|--------------|--|--------------|--------------|
| Model | Backbone | mAP | Model | Backbone | mAP |
| Two-stage or Anchor-based | | | Two-stage or Anchor-based | | |
| APE [†] (Zhu, Du, and Wu 2020) | RX-101 | 75.75 | KLD (RetinaNet) [*] (Yang et al. 2021b) | R-50 | 85.56 |
| OWSR ^{††} (Li et al. 2019a) | R-101 + RX-101 + mdcn-R-101 | 76.36 | KLD (R ³ Det) ^{†*} (Yang et al. 2021b) | R-101 | 87.45 |
| KLD (RetinaNet) [*] (Yang et al. 2021b) | R-50 | 78.32 | ReDet [†] (Han et al. 2021b) | ReR-50+ReFPN | 90.46 |
| ReDet ^{†*} (Han et al. 2021b) | ReR-101+ReFPN | 80.10 | Oriented R-CNN ^{†*} (Xie et al. 2021) | R-101 | 90.50 |
| KLD (R ³ Det) ^{†*} (Yang et al. 2021b) | R-152 | 80.17 | One-stage and Anchor-free | | |
| Oriented R-CNN ^{†*} (Xie et al. 2021) | R-50 | 80.87 | IENet [*] (Lin, Feng, and Guan 2019) | R-101 | 75.01 |
| One-stage and Anchor-free | | | Axis Learning (Xiao et al. 2020) | R-101 | 78.51 |
| IENet [*] (Lin, Feng, and Guan 2019) | R-101 | 57.15 | PloU [*] (Chen et al. 2020) | R-101 | 80.32 |
| PloU [*] (Chen et al. 2020) | DLA-34 | 60.50 | BBAV [*] (Yi et al. 2021) | R-101 | 88.60 |
| Axis Learning (Xiao et al. 2020) | R-101 | 65.98 | PloU [*] (Chen et al. 2020) | DLA-34 | 89.20 |
| P-RSDet [*] (Zhou et al. 2020a) | R-101 | 72.30 | DAFNe [*] | R-101 | 89.51 |
| O ² -DNet (Wei et al. 2020) | HG-104 | 71.04 | DAFNe [*] | R-50 | 89.76 |
| AF-EMS (Yan et al. 2021) | R-101 | 69.86 | MEAD (He et al. 2021b) | R-101 | 89.83 |
| AROA (He et al. 2021a) | R-101 | 75.41 | CenterRot (Wang, Yang, and Li 2021) | R-50 | 90.20 |
| MEAD (He et al. 2021b) | R-101 | 74.80 | | | |
| CenterRot (Wang, Yang, and Li 2021) | R-101 | 74.00 | | | |
| BBAV [*] (Yi et al. 2021) | R-101 | 75.36 | | | |
| CFA [*] (Guo et al. 2021) | R-101 | 75.05 | | | |
| DAFNe [*] | R-50 | 76.73 | | | |
| DAFNe [*] | R-101 | 76.95 | | | |
| (c) Evaluation on DOTA 1.5 | | | (d) Evaluation on UCAS-AOD | | |
| Model | Backbone | mAP | Model | Backbone | mAP |
| Two-stage or Anchor-based | | | Two-stage or Anchor-based | | |
| OWSR ^{††} (Li et al. 2019a) | R-101 + RX-101 + mdcn-R-101 | 76.60 | R-Yolov3 (Redmon and Farhadi 2018) | DN-53 | 82.08 |
| ReDet ^{†*} (Han et al. 2021b) | ReR-50+ReFPN | 78.08 | Faster R-CNN [†] (Ren et al. 2015) | R-50 | 88.86 |
| APE [†] (Zhu, Du, and Wu 2020) | RX-101 | 78.34 | RoI Transformer [†] (Ding et al. 2019) | R-50 | 89.02 |
| One-stage and Anchor-free | | | SLA (Ming et al. 2021a) | R-50 | 89.44 |
| DAFNe [*] | R-50 | 71.47 | CFC-Net (Ming et al. 2022a) | R-50 | 89.49 |
| DAFNe [*] | R-101 | 71.99 | RIDet-O (Ming et al. 2022b) | R-50 | 89.62 |
| | | | DAL (Ming et al. 2021b) | R-50 | 89.87 |
| | | | S2ANet (Han et al. 2021a) | R-50 | 89.99 |
| | | | One-stage and Anchor-free | | |
| | | | R-RetinaNet (Lin et al. 2020) | R-50 | 87.57 |
| | | | DAFNe [*] | R-50 | 89.73 |
| | | | DAFNe [*] | R-101 | 89.85 |

References

- Chen, L.-C.; Papandreou, G.; Schroff, F.; and Adam, H. 2017. Rethinking Atrous Convolution for Semantic Image Segmentation. arXiv preprint arXiv: 1706.05587. arXiv:1706.05587.
- Chen, Z.; Chen, K.-A.; Lin, W.; See, J.; Yu, H.; Ke, Y.; and Yang, C. 2020. PloU Loss: Towards Accurate Oriented Object Detection in Complex Environments. In *European Conference on Computer Vision (ECCV)*.
- Dai, J.; He, K.; and Sun, J. 2016. Instance-Aware Semantic

Segmentation via Multi-task Network Cascades. *Conference on Computer Vision and Pattern Recognition (CVPR)*.

Deng, J.; Dong, W.; Socher, R.; Li, L.-J.; Li, K.; and Fei-Fei, L. 2009. ImageNet: A Large-Scale Hierarchical Image Database. In *Conference on Computer Vision and Pattern Recognition (CVPR)*.

Ding, J.; Xue, N.; Long, Y.; Xia, G.-S.; and Lu, Q. 2019. Learning RoI Transformer for Oriented Object Detection in Aerial Images. In *Conference on Computer Vision and Pattern Recognition (CVPR)*.

- Duan, K.; Bai, S.; Xie, L.; Qi, H.; Huang, Q.; and Tian, Q. 2019. CenterNet: Keypoint Triplets for Object Detection. In *International Conference on Computer Vision (ICCV)*.
- Goodfellow, I.; Bengio, Y.; and Courville, A. 2016. *Deep Learning*. The MIT Press.
- Goyal, P.; Dollár, P.; Girshick, R.; Noordhuis, P.; Wesolowski, L.; Kyrola, A.; Tulloch, A.; Jia, Y.; and He, K. 2018. Accurate, Large Minibatch SGD: Training ImageNet in 1 Hour. arXiv preprint arXiv: 1706.02677. arXiv:1706.02677.
- Guo, Z.; Liu, C.; Zhang, X.; Jiao, J.; Ji, X.; and Ye, Q. 2021. Beyond Bounding-Box: Convex-Hull Feature Adaptation for Oriented and Densely Packed Object Detection. In *Conference on Computer Vision and Pattern Recognition (CVPR)*.
- Han, J.; Ding, J.; Li, J.; and Xia, G.-S. 2021a. Align Deep Features for Oriented Object Detection. *IEEE Trans. on Geoscience and Remote Sensing*.
- Han, J.; Ding, J.; Xue, N.; and Xia, G.-S. 2021b. ReDet: A Rotation-equivariant Detector for Aerial Object Detection. In *Proceedings of the IEEE/CVF Conference on Computer Vision and Pattern Recognition (CVPR)*.
- Hariharan, B.; Arbeláez, P.; Girshick, R.; and Malik, J. 2014. Simultaneous Detection and Segmentation. In *European Conference on Computer Vision (ECCV)*.
- Hariharan, B.; Arbeláez, P.; Girshick, R.; and Malik, J. 2015. Hypercolumns for object segmentation and fine-grained localization. In *Conference on Computer Vision and Pattern Recognition (CVPR)*.
- He, K.; Gkioxari, G.; Dollár, P.; and Girshick, R. 2017. Mask R-CNN. In *International Conference on Computer Vision (ICCV)*.
- He, K.; Zhang, X.; Ren, S.; and Sun, J. 2016. Deep Residual Learning for Image Recognition. In *Conference on Computer Vision and Pattern Recognition (CVPR)*.
- He, X.; Ma, S.; He, L.; Zhang, F.; Liu, X.; and Ru, L. 2021a. AROA: Attention Refinement One-Stage Anchor-Free Detector for Objects in Remote Sensing Imagery. In *Image and Graphics*. Springer International Publishing.
- He, Z.; Ren, Z.; Yang, X.; Yang, Y.; and Zhang, W. 2021b. MEAD: a Mask-guided Anchor-free Detector for oriented aerial object detection. *Applied Intelligence*.
- Kang, K.; Li, H.; Yan, J.; Zeng, X.; Yang, B.; Xiao, T.; Zhang, C.; Wang, Z.; Wang, R.; Wang, X.; and Ouyang, W. 2018. T-CNN: Tubelets With Convolutional Neural Networks for Object Detection From Videos. *IEEE Trans. on Circuits and Systems for Video Technology*, 28.
- Karpathy, A.; and Fei-Fei, L. 2015. Deep visual-semantic alignments for generating image descriptions. In *Conference on Computer Vision and Pattern Recognition (CVPR)*.
- Kong, T.; Sun, F.; Liu, H.; Jiang, Y.; and Shi, J. 2019. FoveaBox: Beyond Anchor-based Object Detector. arXiv preprint arXiv: 1904.03797. arXiv:1904.03797.
- Law, H.; and Deng, J. 2019. CornerNet: Detecting Objects as Paired Keypoints. *International Journal of Computer Vision*.
- Li, C.; Xu, C.; Cui, Z.; Wang, D.; Jie, Z.; Zhang, T.; and Yang, J. 2019a. Learning Object-Wise Semantic Representation for Detection in Remote Sensing Imagery. In *CVPR Workshops*.
- Li, C.; Xu, C.; Cui, Z.; Wang, D.; Zhang, T.; and Yang, J. 2019b. Feature-Attended Object Detection in Remote Sensing Imagery. In *2019 IEEE International Conference on Image Processing (ICIP)*.
- Lin, T.-Y.; Dollár, P.; Girshick, R.; He, K.; Hariharan, B.; and Belongie, S. 2017. Feature Pyramid Networks for Object Detection. In *Conference on Computer Vision and Pattern Recognition (CVPR)*.
- Lin, T.-Y.; Goyal, P.; Girshick, R.; He, K.; and Dollár, P. 2020. Focal Loss for Dense Object Detection. *IEEE Trans. on Pattern Analysis and Machine Intelligence*, 42.
- Lin, Y.; Feng, P.; and Guan, J. 2019. IENet: Interacting Embanchment One Stage Anchor Free Detector for Orientation Aerial Object Detection. arXiv preprint arXiv: 1912.00969. arXiv:1912.00969.
- Liu, L.; Pan, Z.; and Lei, B. 2017. Learning a Rotation Invariant Detector with Rotatable Bounding Box. arXiv preprint arXiv: 1711.09405. arXiv:1711.09405.
- Liu, W.; Anguelov, D.; Erhan, D.; Szegedy, C.; Reed, S. E.; Fu, C.-Y.; and Berg, A. C. 2016. SSD: Single Shot Multi-Box Detector. In *European Conference on Computer Vision (ECCV)*.
- Liu, Z.; Yuan, L.; Weng, L.; and Yang, Y. 2017. A High Resolution Optical Satellite Image Dataset for Ship Recognition and Some New Baselines.
- Ma, J.; Shao, W.; Ye, H.; Wang, L.; Wang, H.; Zheng, Y.; and Xue, X. 2018. Arbitrary-Oriented Scene Text Detection via Rotation Proposals. *IEEE Trans. on Multimedia*, 20.
- Ming, Q.; Miao, L.; Zhou, Z.; and Dong, Y. 2022a. CFC-Net: A Critical Feature Capturing Network for Arbitrary-Oriented Object Detection in Remote-Sensing Images. *IEEE Transactions on Geoscience and Remote Sensing*, 60.
- Ming, Q.; Miao, L.; Zhou, Z.; Song, J.; and Yang, X. 2021a. Sparse Label Assignment for Oriented Object Detection in Aerial Images. *Remote Sensing*, 13.
- Ming, Q.; Miao, L.; Zhou, Z.; Yang, X.; and Dong, Y. 2022b. Optimization for Arbitrary-Oriented Object Detection via Representation Invariance Loss. *IEEE Geoscience and Remote Sensing Letters*, 19.
- Ming, Q.; Zhou, Z.; Miao, L.; Zhang, H.; and Li, L. 2021b. Dynamic Anchor Learning for Arbitrary-Oriented Object Detection. In *Association for the Advancement of Artificial Intelligence (AAAI)*.
- Qian, W.; Yang, X.; Peng, S.; Guo, Y.; and Yan, J. 2021. Learning Modulated Loss for Rotated Object Detection. In *Association for the Advancement of Artificial Intelligence (AAAI)*.
- Redmon, J.; Divvala, S.; Girshick, R.; and Farhadi, A. 2016. You Only Look Once: Unified, Real-Time Object Detection. In *Conference on Computer Vision and Pattern Recognition (CVPR)*.

- Redmon, J.; and Farhadi, A. 2017. YOLO9000: Better, Faster, Stronger. In *Conference on Computer Vision and Pattern Recognition (CVPR)*.
- Redmon, J.; and Farhadi, A. 2018. YOLOv3: An Incremental Improvement. arXiv preprint arXiv: 1804.02767. arXiv:1804.02767.
- Ren, S.; He, K.; Girshick, R.; and Sun, J. 2015. Faster R-CNN: Towards Real-Time Object Detection with Region Proposal Networks. In *Advances in Neural Information Processing Systems (NeurIPS)*.
- Sun, P.; Chen, G.; Luke, G.; and Shang, Y. 2018. Saliency Biased Loss for Object Detection in Aerial Images. arXiv preprint arXiv: 1810.08103. arXiv:1810.08103.
- Tian, Z.; Shen, C.; Chen, H.; and He, T. 2019. FCOS: Fully Convolutional One-Stage Object Detection. In *International Conference on Computer Vision (ICCV)*.
- Wang, J.; Yang, L.; and Li, F. 2021. Predicting Arbitrary-Oriented Objects as Points in Remote Sensing Images. *Remote Sensing*, 13.
- Wei, H.; Zhang, Y.; Chang, Z.; Li, H.; Wang, H.; and Sun, X. 2020. Oriented objects as pairs of Middle Lines. *ISPRS Journal of Photogrammetry and Remote Sensing*, 169.
- Wu, Q.; Shen, C.; Wang, P.; Dick, A.; and van den Hengel, A. 2018. Image Captioning and Visual Question Answering Based on Attributes and External Knowledge. *IEEE Trans. on Pattern Analysis and Machine Intelligence*, 40.
- Xia, G.-S.; Bai, X.; Ding, J.; Zhu, Z.; Belongie, S.; Luo, J.; Dacu, M.; Pelillo, M.; and Zhang, L. 2018. DOTA: A Large-Scale Dataset for Object Detection in Aerial Images. In *Conference on Computer Vision and Pattern Recognition (CVPR)*.
- Xiao, Z.; Qian, L.; Shao, W.; Tan, X.; and Wang, K. 2020. Axis Learning for Orientated Objects Detection in Aerial Images. *Remote Sensing*, 12.
- Xie, X.; Cheng, G.; Wang, J.; Yao, X.; and Han, J. 2021. Oriented R-CNN for Object Detection. *International Conference on Computer Vision (ICCV)*.
- Xu, K.; Ba, J.; Kiros, R.; Cho, K.; Courville, A.; Salakhudinov, R.; Zemel, R.; and Bengio, Y. 2015. Show, Attend and Tell: Neural Image Caption Generation with Visual Attention. In *International Conference on Machine Learning (ICML)*, volume 37.
- Yan, J.; Zhao, L.; Diao, W.; Wang, H.; and Sun, X. 2021. AF-EMS Detector: Improve the Multi-Scale Detection Performance of the Anchor-Free Detector. *Remote Sensing*, 13.
- Yang, X.; Liu, Q.; Yan, J.; and Li, A. 2021a. R3Det: Refined Single-Stage Detector with Feature Refinement for Rotating Object. In *Association for the Advancement of Artificial Intelligence (AAAI)*.
- Yang, X.; and Yan, J. 2020. Arbitrary-Oriented Object Detection with Circular Smooth Label. *European Conference on Computer Vision (ECCV)*.
- Yang, X.; Yan, J.; Yang, X.; Tang, J.; Liao, W.; and He, T. 2020. SCRDet++: Detecting Small, Cluttered and Rotated Objects via Instance-Level Feature Denoising and Rotation Loss Smoothing. arXiv preprint arXiv: 2004.13316. arXiv:2004.13316.
- Yang, X.; Yang, X.; Yang, J.; Ming, Q.; Wang, W.; Tian, Q.; and Yan, J. 2021b. Learning High-Precision Bounding Box for Rotated Object Detection via Kullback-Leibler Divergence. *Advances in Neural Information Processing Systems (NeurIPS)*.
- Yi, J.; Wu, P.; Liu, B.; Huang, Q.; Qu, H.; and Metaxas, D. N. 2021. Oriented Object Detection in Aerial Images with Box Boundary-Aware Vectors. *Winter Conference on Applications of Computer Vision (WACV)*.
- Yu, J.; Jiang, Y.; Wang, Z.; Cao, Z.; and Huang, T. 2016. UnitBox: An Advanced Object Detection Network. In *Proceedings of ACM International Conference on Multimedia*.
- Zhou, L.; Wei, H.; Li, H.; Zhao, W.; Zhang, Y.; and Zhang, Y. 2020a. Arbitrary-Oriented Object Detection in Remote Sensing Images Based on Polar Coordinates. *IEEE Access*.
- Zhou, L.; Wei, H.; Li, H.; Zhao, W.; Zhang, Y.; and Zhang, Y. 2020b. Objects detection for remote sensing images based on polar coordinates. arXiv preprint arXiv: 2001.02988. arXiv:2001.02988.
- Zhou, X.; Zhuo, J.; and Krähenbühl, P. 2019. Bottom-up Object Detection by Grouping Extreme and Center Points. In *Conference on Computer Vision and Pattern Recognition (CVPR)*.
- Zhou, Y.; Ye, Q.; Qiu, Q.; and Jiao, J. 2017. Oriented Response Networks. In *Conference on Computer Vision and Pattern Recognition (CVPR)*.
- Zhu, Y.; Du, J.; and Wu, X. 2020. Adaptive Period Embedding for Representing Oriented Objects in Aerial Images. *IEEE Transactions on Geoscience and Remote Sensing*, 58.

Appendix

A DAFNe Architecture

DAFNe is a one-stage anchor-free model for oriented object detection. It is faster and easier to optimize than two-stage solutions and it does not require predefined anchors as its anchor-based counterparts. To date, it is the most accurate one-stage anchor-free model on DOTA 1.0, DOTA 1.5, and UCAS-AOD. DAFNe architecture can be divided into three parts: 1) The backbone network, ResNet, which is pre-trained to perform image classification on a large dataset such as ImageNet, thus, it is able to extract meaningful and robust intermediate deep feature maps, 2) the Feature Pyramid Network which can construct feature pyramids from the backbone feature maps using lateral top-down and bottom-up connections with marginal cost and 3) the task-specific heads which are separate sequential convolution branches on top of the FPN output that produce predictions for different task objectives. A comprehensive illustration of the architecture can be found in Figure 6.

In particular, the FPN extracts three feature maps, namely C_3 , C_4 , and C_5 from the ResNet backbone. As outlined in Figure 6, P_3 , P_4 , and P_5 are constructed using C_3 , C_4 , and C_5 while connecting P_5 with P_4 as well as P_4 with P_3 using lateral connections in a top-down fashion using nearest-neighbor upsampling and 1×1 convolutions. Pyramid level P_6 is obtained using a 3×3 convolution with stride

2 on P_5 , while level P_7 is obtained using a 3×3 convolution with stride 2 and a ReLU activation on P_6 . Each pyramid level has an additional 3×3 output convolution with 256 channels. This results in five FPN output feature maps $\{P_3, P_4, P_5, P_6, P_7\}$ with dimensions $\frac{H}{2^l} \times \frac{W}{2^l} \times 256$ for output P_l at level l . The different feature maps serve as deep representations of the input at different spatial resolutions. Each feature in P_l is responsible for patches of

$$\frac{H}{2^l} \times \frac{W}{2^l} = 2^l \times 2^l$$

pixels in the network input. In the context of object detection, this means that each feature map P_l is responsible for a different object size. Figure 7 shows the mapping of feature map responsibilities for each FPN output level onto an exemplary blank image as input image of size 128×128 .

Finally, the last architectural section, also called the *head*, takes care of the task-specific objectives. For this, each objective is being assigned to a single branch in the head. A branch starts with a convolution tower, i.e. a sequence of multiple 3×3 convolution layers that retain the spatial dimensions of their input by padding the sides accordingly. On top of the convolution tower, a task-specific 3×3 prediction convolution is placed to map the tower outputs to the task-specific values. In this work, we employ two branches as depicted in the rightmost section of Figure 6.

The first branch generates a $H \times W \times |C|$ class prediction output, where $|C|$ corresponds to the number of classes present in the dataset. In other words, for each location in the spatial grid of size $H \times W$, the network generates a logits vector of length $|C|$ that indicates the class of a possible object at that location, taking into account also that there might not be an object. In this case, this outcome is filtered out by employing a simple class score threshold later on.

The second branch produces a $H \times W \times 8$ coordinate regression output, where each vector of length 8 in the $H \times W$ output map corresponds to an oriented bounding box represented as quadrilateral of its four corner points $(x_0, y_0, x_1, y_1, x_2, y_2, x_3, y_3)$. Each coordinate is interpreted as an offset vector relative to the location at which the prediction occurs. Furthermore, a second $H \times W \times 1$ oriented center-ness prediction is realized, which is then transformed into normalized oriented center-ness values using the sigmoid transformation.

B Class-based Oriented Center-Ness Heatmaps

We have collected the true positive detections as a heatmap to better understand how the oriented center-ness improves the model accuracy. The classification confidences for the 15 different classes of the DOTA 1.0 validation set, obtained without oriented center-ness are depicted in Figure 8, while the ones obtained with oriented center-ness are in Figure 9.

The detection classification confidences are drawn against the Intersection over Union (IoU) with the ground-truth bounding box. For each correctly detected oriented bounding box in the validation set, a pair of (*confidence*, *IoU*)

is collected, where the IoU is computed between the predicted bounding box and the ground-truth bounding box. The heatmap brightness indicates the density of correctly detected objects in the validation dataset. For a fair comparison, the values used for the heatmaps are the confidences p and not the center-ness adjusted scores s . The inclusion of oriented center-ness during training as an adjustment to the classification confidence results in detections of higher confidences (and better IoU) already before scaling them with the oriented center-ness value. This is appreciable in almost all the classes. In this way, the detections with low center-ness values are correctly removed during post-processing steps such as score thresholding and non-maximum suppression. Moreover, the results obtained on classes such as “helicopter” indicate that future works could explore how to combine two or more center-ness functions in a fashion similar to “Mixture of Experts”.

C DOTA 1.0 Evaluations per Class and Predictions Illustration

DAFNe with oriented center-ness and center-to-corner prediction strategy sets the new state-of-the-art accuracy result on DOTA 1.0. Table 4 shows the class-separated test accuracy (in mAP) achieved by DAFNe and all its one-stage anchor-free competitors in the literature, to the best of our knowledge, and by more complex two-stage and anchor-based models. DAFNe improves accuracy over the previous state-of-the-art in 7 out of 15 classes and it is either second best or close to the best scoring model for all other classes. The acronyms refer to the following classes: PL plane, BD baseball-diamond, BR bridge, GTF ground-track-field, SH small-vehicle, LV large-vehicle, ST ship, TC tennis-court, BC basketball-court, ST storage-tank, SBF soccer-ball-field, RA roundabout, HA harbour, SP swimming-pool, HC helicopter.

Figure 10 and Figure 11 show accurate object predictions on some DOTA 1.0 validation set samples performed by DAFNe. During our experiments, we also have investigated how much DAFNe is sensitive to random seeds. We have computed the DOTA 1.0 validation accuracy by using 10 different seeds obtaining a negligible standard deviation of only 0.05%, therefore, DAFNe is not sensitive to random seeds.

Table 4: Test set accuracies on DOTA 1.0 (in mAP) of DAFNe compared with all other one-stage anchor-free oriented object detection models in the literature and with more complex two-stage and anchor-based models. Note that “*” indicates multi-scale training and testing, and “†” indicates a two-stage model. Best results in bold, our approach is highlighted. Our model improves over the previous state-of-the-art in 7 out of 15 classes and it is either second best or close to the best scoring model for all other classes

| Method | PL | BD | BR | GTF | SV | LV | SH | TC |
|--|--------------|--------------|--------------|--------------|--------------|--------------|--------------|--------------|
| Two-stage or Anchor-based | | | | | | | | |
| APE ^{*†} (Zhu, Du, and Wu 2020) | 89.96 | 83.62 | 53.42 | 76.03 | 74.01 | 77.16 | 79.45 | 90.83 |
| OWSR ^{*†} (Li et al. 2019a) | 90.41 | 85.21 | 55.00 | 78.27 | 76.19 | 72.19 | 82.14 | 90.70 |
| KLD (RetinaNet) [*] (Yang et al. 2021b) | 88.91 | 85.23 | 53.64 | 81.23 | 78.20 | 76.99 | 84.58 | 89.50 |
| ReDet ^{*†} (Han et al. 2021b) | 88.81 | 82.48 | 60.83 | 80.82 | 78.34 | 86.06 | 88.31 | 90.87 |
| KLD (R ³ Det) ^{*†} (Yang et al. 2021b) | 89.92 | 85.13 | 59.19 | 81.33 | 78.82 | 84.38 | 87.50 | 89.80 |
| Oriented R-CNN ^{*†} (Xie et al. 2021) | 89.84 | 85.43 | 61.09 | 79.82 | 79.71 | 85.35 | 88.82 | 90.88 |
| One-stage and Anchor-free | | | | | | | | |
| IENet [*] (Lin, Feng, and Guan 2019) | 88.15 | 71.38 | 34.26 | 51.78 | 63.78 | 65.63 | 71.61 | 90.11 |
| PIoU [*] (Chen et al. 2020) | 80.90 | 69.70 | 24.10 | 60.20 | 38.30 | 64.40 | 64.80 | 90.90 |
| AxisLearning (Xiao et al. 2020) | 79.53 | 77.15 | 38.59 | 61.15 | 67.53 | 70.49 | 76.30 | 89.66 |
| AF-EMS (Yan et al. 2021) | 93.11 | 73.70 | 48.95 | 63.03 | 50.85 | 75.65 | 91.54 | 92.57 |
| O ² -DNet (Wei et al. 2020) | 89.31 | 82.14 | 47.33 | 61.21 | 71.32 | 74.03 | 78.62 | 90.76 |
| P-RSDet [*] (Zhou et al. 2020a) | 88.58 | 77.84 | 50.44 | 69.29 | 71.10 | 75.79 | 78.66 | 90.88 |
| CenterRot [*] (Wang, Yang, and Li 2021) | 89.74 | 83.57 | 49.53 | 66.45 | 77.07 | 80.57 | 86.97 | 90.75 |
| MEAD (He et al. 2021b) | 88.42 | 79.00 | 49.29 | 68.76 | 77.41 | 77.68 | 86.60 | 90.78 |
| CFA [*] (Guo et al. 2021) | 89.26 | 81.72 | 51.81 | 67.17 | 79.99 | 78.25 | 84.46 | 90.77 |
| BBAV [*] (Yi et al. 2021) | 88.63 | 84.06 | 52.13 | 69.56 | 78.26 | 80.40 | 88.06 | 90.87 |
| AROA (He et al. 2021a) | 88.33 | 82.73 | 56.02 | 71.58 | 72.98 | 77.59 | 78.29 | 88.63 |
| DAFNe [*] | 89.40 | 86.27 | 53.70 | 60.51 | 82.04 | 81.17 | 88.66 | 90.37 |
| | BC | ST | SBF | RA | HA | SP | HC | mAP |
| Two-stage or Anchor-based | | | | | | | | |
| APE ^{*†} (Zhu, Du, and Wu 2020) | 87.15 | 84.51 | 67.72 | 60.33 | 74.61 | 71.84 | 65.55 | 75.75 |
| OWSR ^{*†} (Li et al. 2019a) | 87.22 | 86.87 | 66.62 | 68.43 | 75.43 | 72.70 | 57.99 | 76.36 |
| KLD (RetinaNet) [*] (Yang et al. 2021b) | 86.84 | 86.38 | 71.69 | 68.06 | 75.95 | 72.23 | 75.42 | 78.32 |
| ReDet ^{*†} (Han et al. 2021b) | 88.77 | 87.03 | 68.65 | 66.90 | 79.26 | 79.71 | 74.67 | 80.10 |
| KLD (R ³ Det) ^{*†} (Yang et al. 2021b) | 87.33 | 87.00 | 72.57 | 71.35 | 77.12 | 79.34 | 78.68 | 80.63 |
| Oriented R-CNN ^{*†} (Xie et al. 2021) | 86.68 | 87.73 | 72.21 | 70.80 | 82.42 | 78.18 | 74.11 | 80.87 |
| One-stage and Anchor-free | | | | | | | | |
| IENet [*] (Lin, Feng, and Guan 2019) | 71.07 | 73.63 | 37.62 | 41.52 | 48.07 | 60.53 | 49.53 | 61.24 |
| PIoU [*] (Chen et al. 2020) | 77.20 | 70.40 | 46.50 | 37.10 | 57.10 | 61.90 | 64.00 | 60.50 |
| AxisLearning (Xiao et al. 2020) | 79.07 | 83.53 | 47.27 | 61.01 | 56.28 | 66.06 | 36.05 | 65.98 |
| AF-EMS (Yan et al. 2021) | 59.29 | 73.17 | 49.87 | 69.00 | 81.79 | 66.99 | 58.33 | 69.86 |
| O ² -DNet (Wei et al. 2020) | 82.23 | 81.36 | 60.93 | 60.17 | 58.21 | 66.98 | 61.03 | 71.04 |
| P-RSDet [*] (Zhou et al. 2020a) | 80.10 | 81.71 | 57.92 | 63.03 | 66.30 | 69.77 | 63.13 | 72.30 |
| CenterRot (Wang, Yang, and Li 2021) | 81.50 | 84.05 | 54.14 | 64.14 | 74.22 | 72.77 | 54.56 | 74.00 |
| MEAD (He et al. 2021b) | 85.55 | 84.54 | 62.10 | 66.57 | 72.59 | 72.84 | 59.83 | 74.80 |
| CFA [*] (Guo et al. 2021) | 83.40 | 85.54 | 54.86 | 67.75 | 73.04 | 70.24 | 64.96 | 75.05 |
| BBAV [*] (Yi et al. 2021) | 87.23 | 86.39 | 56.11 | 65.62 | 67.10 | 72.08 | 63.96 | 75.36 |
| AROA (He et al. 2021a) | 83.33 | 86.61 | 65.93 | 63.52 | 76.03 | 78.43 | 61.33 | 75.41 |
| DAFNe [*] | 83.81 | 87.27 | 53.93 | 69.38 | 75.61 | 81.26 | 70.86 | 76.95 |

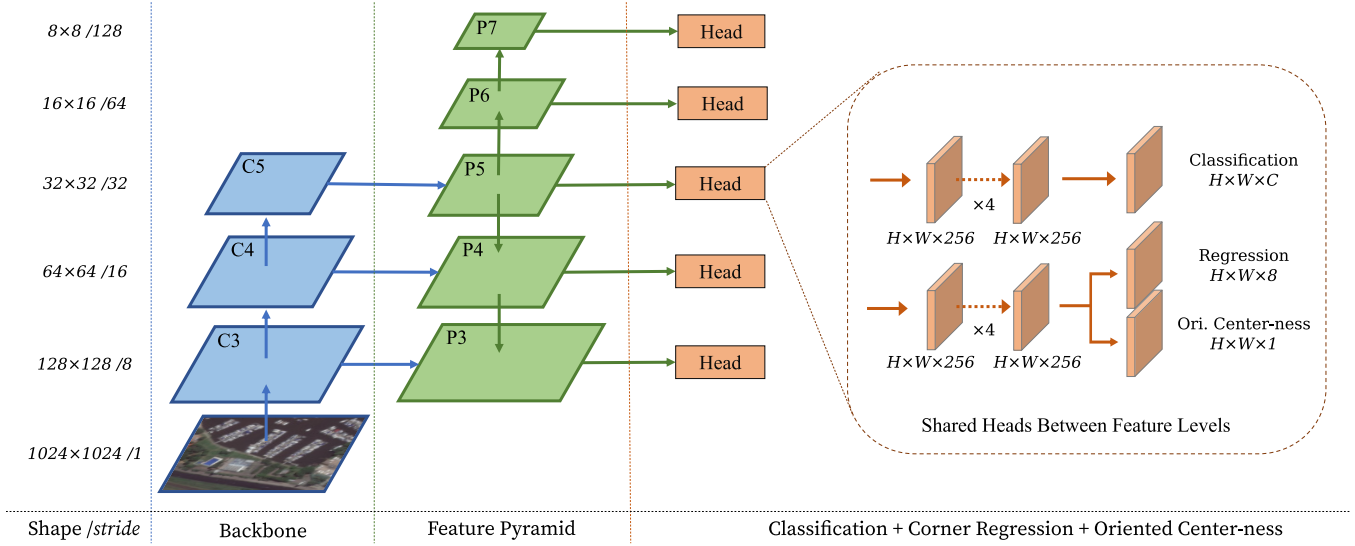


Figure 6: The main network architecture of DAFNe. $H \times W$ denotes the height and width of the feature maps and $/s$ is the down-sampling ratio w.r.t. the input size, also called *stride*. The model uses feature maps $C3$, $C4$, and $C5$ of the backbone network, feeds them into levels $P3$ - 5 of the FPN and uses $P3$ - 7 for the final prediction of class confidences, object location, and oriented center-ness. The depiction is a modification of the one presented in (Tian et al. 2019).

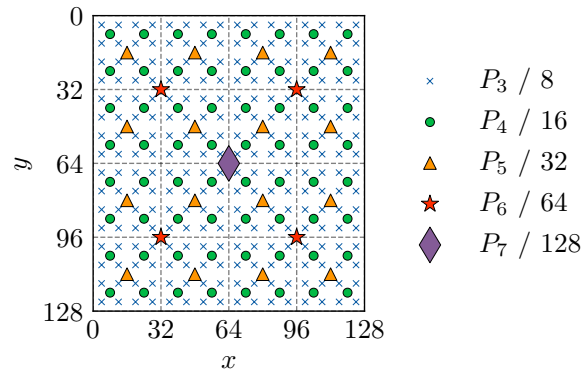


Figure 7: Feature map responsibilities w.r.t. an exemplary 128×128 pixel image input for FPN outputs $\{P_3, P_4, P_5, P_6, P_7\}$ with their respective strides. For example, P_5 has an output stride $s = 32$, thus, a single feature in P_5 covers a block of 32×32 pixels in the input image, resulting in $\frac{128}{32} \cdot \frac{128}{32} = 16$ features per channel. A feature map location (x, y) can be mapped back onto the input image as follows: $(\lfloor \frac{s}{2} \rfloor + xs, \lfloor \frac{s}{2} \rfloor + ys)$.

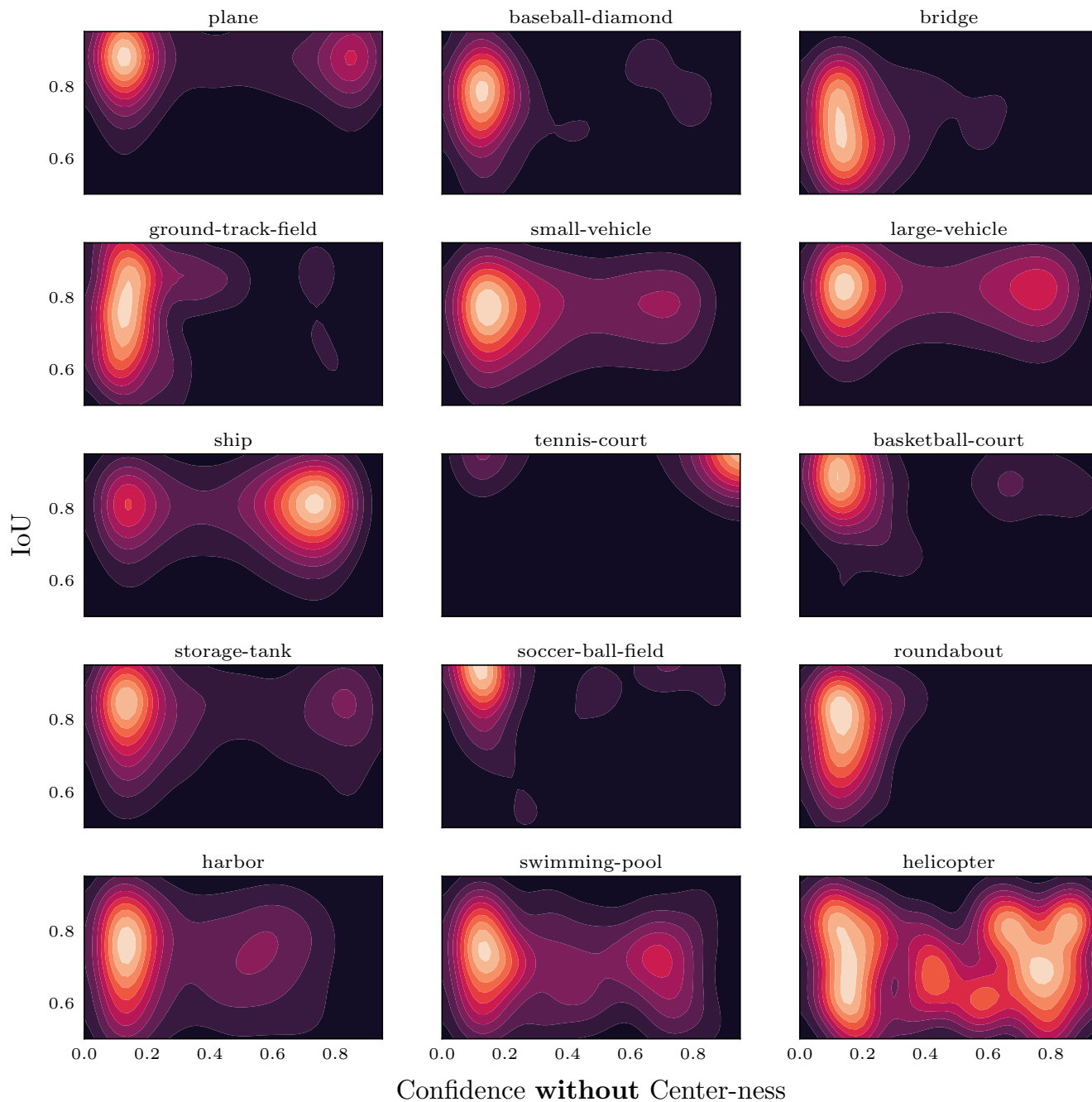
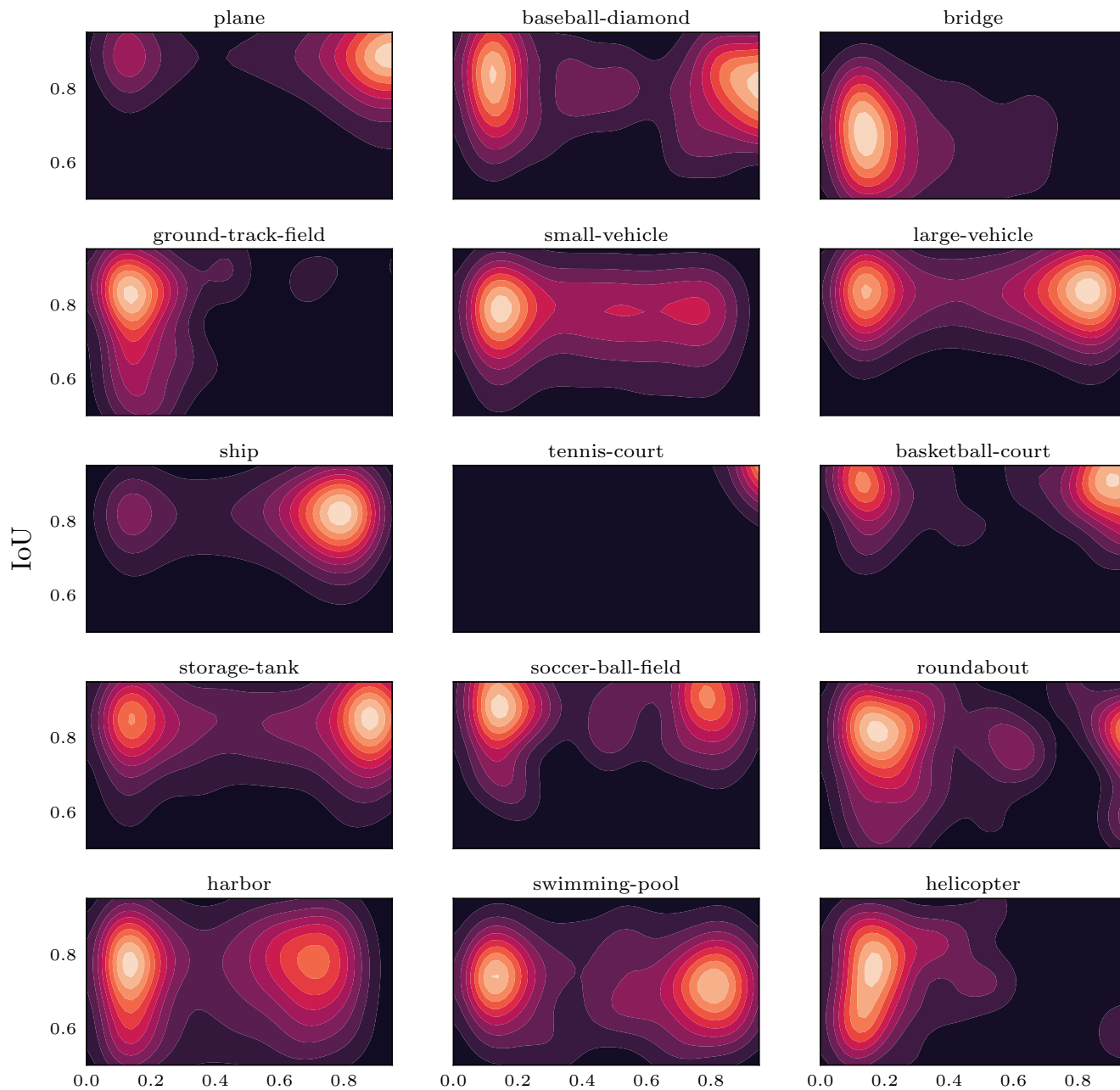


Figure 8: Heatmaps of classification confidences against IoU values for correctly detected oriented bounding boxes in the DOTA 1.0 validation set (true positives). Values are obtained from a model without oriented center-ness. In most of the classes the confidence concentrates around 0.1 and 0.2. This increases the chance that correct detections are wrongly discarded in the post-processing steps.



Confidence **with** Oriented Center-ness

Figure 9: Heatmaps of classification confidences against IoU values for correctly detected oriented bounding boxes in the DOTA 1.0 validation set (true positives). Values are obtained from a model with oriented center-ness which results in higher classification confidence for correct detections and lower for the wrong ones. In this way, it is more likely that the wrong detections will be correctly removed in the post-processing steps.



Figure 10: Accurate object predictions on some DOTA 1.0 validation set samples performed by DAFNe. In each couple of images, the left one shows object localizations and classifications with annotated confidence values, the right one shows the ground-truth objects positions and classes.

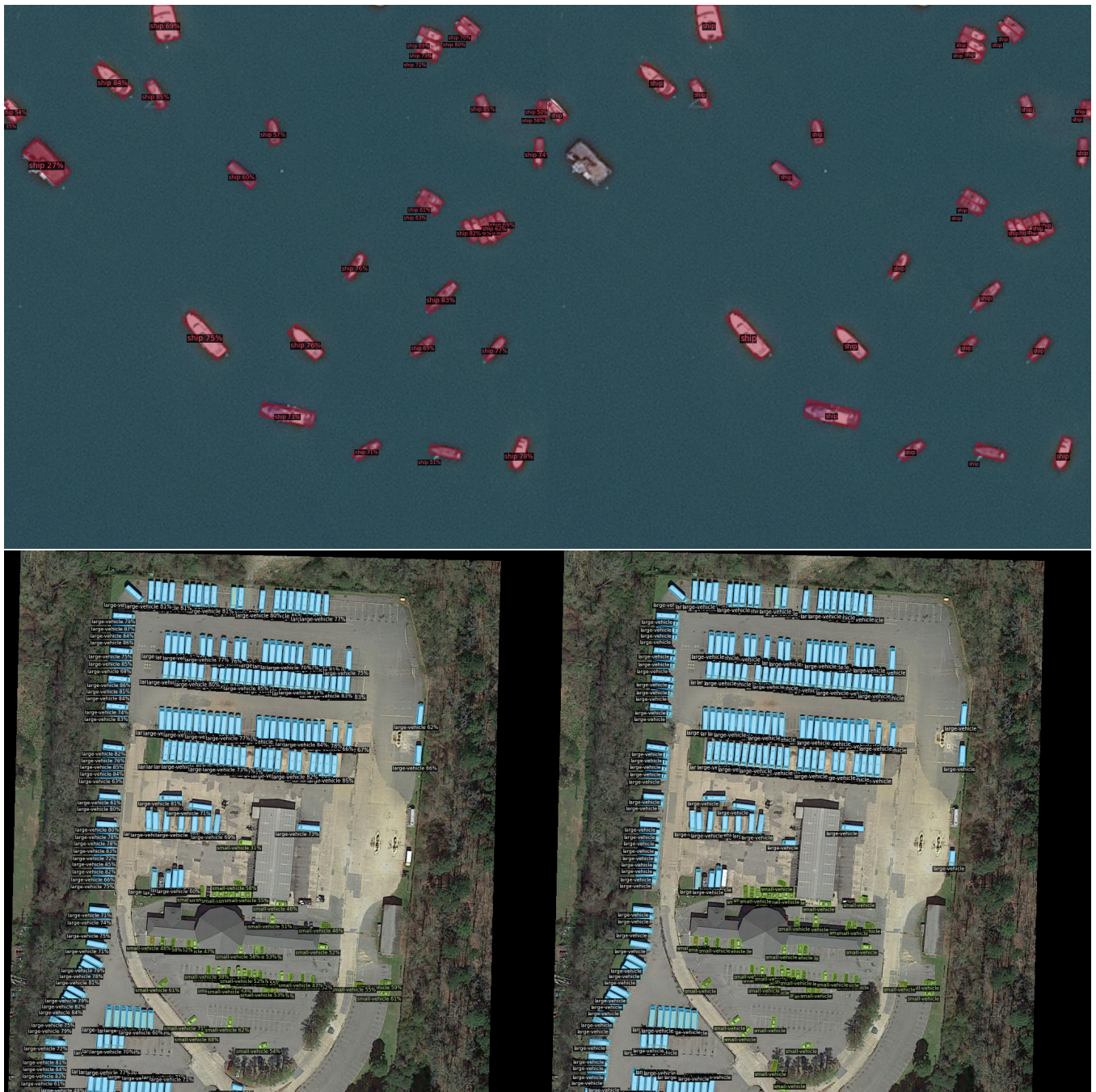


Figure 11: Accurate object predictions on some DOTA 1.0 validation set samples performed by DAFNe. In each couple of images, the left one shows object localizations and classifications with annotated confidence values, the right one shows the ground-truth objects positions and classes.